Coherent structures in the inner part of a rough-wall channel flow resolved using holographic PIV

Siddharth Talapatra and Joseph Katz†

The Johns Hopkins University, Baltimore, MD 21218, USA

Microscopic holographic PIV performed in an optically index-matched facility resolves the three-dimensional flow in the inner part of a turbulent channel flow over a rough wall at Reynolds number $Re_\tau = 3520$. The roughness consists of uniformly distributed pyramids with normalized height of $k_s^+ = 1.5k^+ = 97$. Distributions of mean flow and Reynolds stresses agree with two-dimensional PIV data except very close to the wall ($<0.7k$) owing to the higher resolution of holography. Instantaneous realizations reveal that the roughness sublayer is flooded by low-lying spanwise and groove-parallel vortical structures, as well as quasi-streamwise vortices, some quite powerful, that rise at sharp angles. Conditional sampling and linear stochastic estimation (LSE) reveal that the prevalent flow phenomenon in the roughness sublayer consists of interacting U-shaped vortices, conjectured in Hong *et al.* (*J. Fluid Mech.*, 2012, doi:10.1017/jfm.2012.403). Their low-lying base with primarily spanwise vorticity is located above the pyramid ridgeline, and their inclined quasi-streamwise legs extend between ridgelines. These structures form as spanwise vorticity rolls up in a low-speed region above the pyramid's forward face, and is stretched axially by the higher-speed flow between ridgelines. Ejection induced by interactions among legs of vortices generated by neighbouring pyramids appears to be the mechanism that lifts the quasi-streamwise vortex legs and aligns them preferentially at angles of 54°–63° to the streamwise direction.

Key words: boundary layer structure, turbulent boundary layers

---

1. Introduction

Predicting the effect of roughness geometry on turbulence in rough-wall boundary layers has been a major challenge, for which we only have partial answers (Jimenez 2004). Outside of the 'roughness sublayer', which extends to 2–5 roughness heights (k) away from the surface, a large body of literature (but not all) has indicated that many of the flow features become 'universal', following the so-called Townsend's similarity hypothesis (Raupach, Antonia & Rajagopalan 1991). The turbulence within the roughness sublayer is much less understood. Relevant direct numerical simulation (DNS) studies have been limited to low Reynolds numbers or two-dimensional roughness (e.g. Ikeda & Durbin 2007). Owing to difficulties in recording data near rough surfaces, most experimental studies have stayed away from the wall

† Email address for correspondence: katz@jhu.edu

(e.g. Tachie, Bergstrom & Balachandar 2003; Schultz & Flack 2009), and those that have ventured into the sublayer have been limited to flow visualizations or sparse roughness geometries (Monty *et al.* 2011). However, by performing two-dimensional particle-image velocimetry (PIV) measurements in an optically index-matched facility, Hong, Katz & Schultz (2011) covered the entire roughness sublayer of a turbulent channel flow over a dense three-dimensional rough wall. They showed, consistent with Ikeda & Durbin (2007), that the turbulence production, dissipation and wall-normal transport rates peaked near the top of the roughness. They also showed that although the Reynolds stress distribution agreed with the similarity hypothesis outside the sublayer, energy and shear spectra indicated that eddies generated at the wall with characteristic sizes of k–$3k$ flooded the outer layer, even at $y/k = 20$. In a follow-up work, Hong *et al.* (2012) spatially filtered their data, at scales of k–$6k$, to examine the energy transfer across turbulence scales, the subgrid-scale (SGS) energy flux. Based on a statistical analysis of the vortex configuration, they showed that the SGS flux was dominated by coherent structures bearing clear roughness signature well above the sublayer. Furthermore, a few intense structures, present only in (e.g.) 5 % of the realizations, were responsible for most (>50 %) of the flux. Phenomena revealed by conditional sampling of the two-dimensional data, based on high SGS fluxes, led them to postulate that the intense events were associated with abrupt lifting of U-shaped vortices. These structures were generated as turbulence interacted with the roughness elements.

In this paper, we perform high-resolution, three-dimensional velocity measurements, using digital holographic microscopy, to examine the three-dimensional flow structures within the same roughness sublayer as Hong *et al.* (2012). Conditional sampling and linear stochastic estimation (LSE)-based analysis prove that U-shaped vortices indeed exist, and elucidate the mechanisms involved in their formation and lifting away from the wall at a sharp angle to the streamwise direction.

2. Experimental setup

Experiments have been performed in a 3.3 m long, acrylic rectangular channel with a 20 cm × 5 cm cross-section under the same conditions as described in Hong *et al.* (2011, 2012). This channel contains a concentrated solution of NaI in water, 62 % by weight, to match the refractive index of the acrylic walls. Two 1.25 m long rough plates are inserted symmetrically in the bottom and top walls of the downstream part of the channel. The Reynolds number based on centreline velocity (U) and half channel height (h) is 62 500, the friction velocity (u_τ) is 0.155 m s^{-1}, the wall unit is 7.3 μm, and the friction velocity Reynolds number, Re_τ is 3520. The wall stress is estimated by extrapolating the total shear stress distribution to the wall, using the two-dimensional PIV data (Hong *et al.* 2011). The roughness (figure 1*a*) consists of uniformly distributed, closely packed square pyramids, with $k = 0.46$ mm, and wavelength (λ) of 3.2 mm ($\lambda/k = 6.95$). Here, $h/k = 54$, and $k^+ = ku_\tau/\nu = 65$ (where ν is fluid viscosity), i.e. the boundary layer is well-characterized (Jimenez 2004). Also, based on Schultz & Flack (2009), $k_s = 1.5k$. The sample volume is located 36h downstream of the beginning of the rough wall, 110h from the beginning of the channel. Based on Hong *et al.* (2011), consistent with Antonia & Luxton (1971), fully developed rough channel flow conditions exist in the sample area.

The volumetric velocity distribution is measured using in-line digital holographic microscopy (Sheng, Malkiel & Katz 2006) using the setup illustrated in figure 1(*b*). Light from a pulsed Nd-YAG Laser (532 nm), with an inter-frame time of 25 μs, and
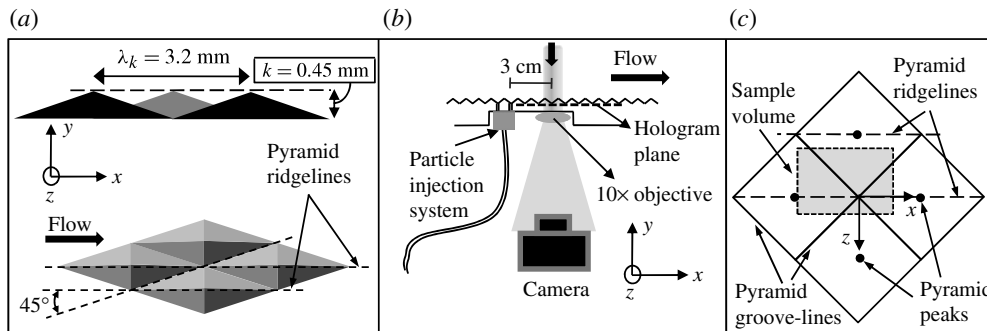
FIGURE 1. (*a*) Roughness geometry; (*b*) coordinate system and experimental setup for recording in-line microscopic holograms in the rough channel; and (*c*) top view of sample volume.

a repetition rate of 1 pulse pair per second, is spatially filtered and collimated before illuminating the test section from above. Part of this beam is scattered by particles located in the path of the beam and interferes with the remaining beam to form a hologram. Index-matching enables the beam to pass through the rough walls with little distortion. The hologram is magnified by a $10\times$ objective and recorded by a 4864×3248 pixel interline transfer camera, providing a 3.3 mm $\times 2.2$ mm field of view, with 0.67 μm pixel^{-1} resolution. To achieve dense particle seeding near the wall, we inject 2 μm silver–coated glass particles from 100 μm holes located 3 cm upstream of the field of view (figure 1*b*). Maintaining a low injection speed of $0.03U$, and keeping the injectors 300 diameters upstream of the sample area minimizes their effect on the flow. Hologram pairs containing 5000–10 000 matched particle pairs are utilized for measuring three-dimensional velocity fields.

The present image processing and particle tracking procedures are detailed in Talapatra & Katz (2012). Following Sheng, Malkiel & Katz (2008), the holograms are reconstructed numerically in 4 μm wall-normal steps, followed by three-dimensional segmentation to obtain a list of particles and their three-dimensional coordinates, and particle tracking to determine their three-dimensional velocity. The tracking algorithm utilizes seven criteria for matching traces, e.g. particle size and volume, planar PIV to provide guess vectors, spatial smoothness of the vector field, etc. In addition, we use edge detection to reassess the wall-normal location of the particles, which refines the three-dimensional segmentation results. In the current dataset, 5000–7000 particles are detected and tracked to obtain the corresponding unstructured three-dimensional velocity vectors in a 3.1 mm $\times 2.1$ mm $\times 1.8$ mm sample volume, the long dimension being in the streamwise direction and the shortest in the spanwise direction. The unstructured vector field is interpolated to a uniform three-dimensional grid using a second-order Taylor series expansion and singular value decomposition (SVD), which provides the velocity and its spatial gradients. The interpolated data at each grid point are based on the velocity of particle pairs located within an ellipsoid with dimensions of 300 μm ($0.67k$) in the streamwise direction and 180 μm ($0.4k$) in the other directions. Only grid points with at least 10 unstructured vectors within the ellipsoid are utilized. With overlap among neighbouring volumes, the structured vector spacing is 60 μm along all three dimensions. We measure the flow from 90 μm below the peak of the pyramid ($y/k = -0.2$) to 2400 μm above the peak ($y/k = 4.33$), where $y = 0$ is defined at the pyramid peak. A detailed uncertainty analysis, based in part
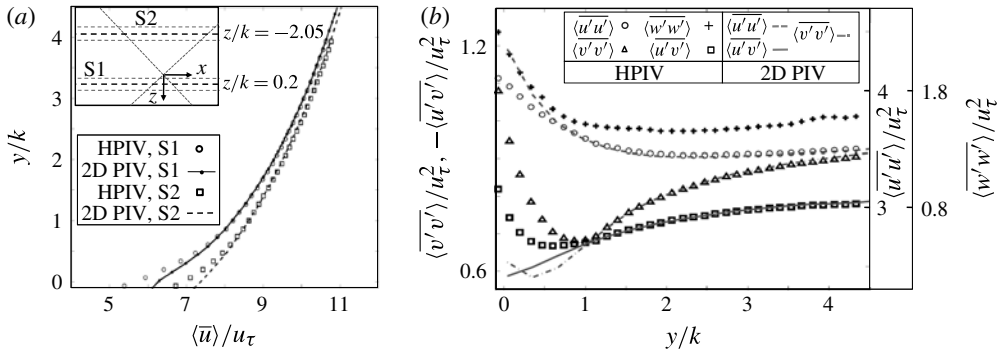
FIGURE 2. (*a*) A comparison of the HPIV mean velocity profiles averaged over a 0.5 mm spanwise interval around S1 and S2 (see inset), to two-dimensional PIV data (Hong *et al.* 2011); and (*b*) spatially averaged Reynolds stress profiles for S1. Note the different scales.

on how well the data satisfy the continuity equation, is discussed in Talapatra & Katz (2012). We compare the three-dimensional data to the available two-dimensional data in the following section. In presenting the data, u, v and w are the velocity components and ω_x, ω_y and ω_z are the vorticity components in the x-, y- and z-directions, respectively, u' is the fluctuating component, and $\langle \rangle$ denotes ensemble averaging.

3. Results

3.1. *Mean flow profiles and Reynolds stresses*

Figure 2(*a*) compares the two-dimensional data obtained by Hong *et al.* (2011) to the holographic PIV (HPIV) based $\overline{\langle u \rangle}$, where the overbar indicates spatial averaging over two different spanwise slices, denoted S1 and S2 in the inset. Each slice is 0.5 mm wide to be consistent with the effective thickness of the two-dimensional PIV data. The two data sets collapse for $y/k > 0.5$, but at lower elevations, the present velocity is persistently lower, with the difference peaking at the roughness top. Owing to the pyramid-induced flow channelling, the near-wall velocity along S1, which is nearly aligned with the ridgeline, is lower than that along S2, which is located between the ridgelines. Figure 2(*b*) compares profiles of Reynolds stresses spatially averaged over S1 and S2, after ensemble averaging at each point. All the present stress components rise sharply as the wall is approached, consistent with Ikeda & Durbin (2007). Both $\overline{\langle u'v' \rangle}$ and $\overline{\langle v'v' \rangle}$ have minima at $0.5 < y/k < 1$, while $\overline{\langle u'u' \rangle}$ and $\overline{\langle w'w' \rangle}$ have broad mild minima around $y/k = 2$. The present profile of $\overline{\langle u'u' \rangle}$ deviates from the two-dimensional data only at $y/k < 0.5$, where the differences are at most 5 %. The two- and three-dimensional profiles of $\overline{\langle u'v' \rangle}$ and $\overline{\langle v'v' \rangle}$ collapse at $y/k > 0.7$, but deviate closer to the wall. There are two causes for the discrepancies between the two- and three-dimensional data near the wall (Talapatra & Katz 2012). First, in two-dimensional PIV, the correlations provide a simple average of particle displacement in the interrogation window. Conversely, the present interpolation of particle tracks onto a regular grid accounts for the location of each particle, effectively increasing the resolution. Also, since the measured seed particle concentration increases with distance from the wall, simple averaging overestimates the near-wall velocity. Indeed, replacing the interpolation with simple averaging reduces the discrepancy from 7 % to 1.2 %. Second, the resolution of two-dimensional PIV is lower than that of the three-
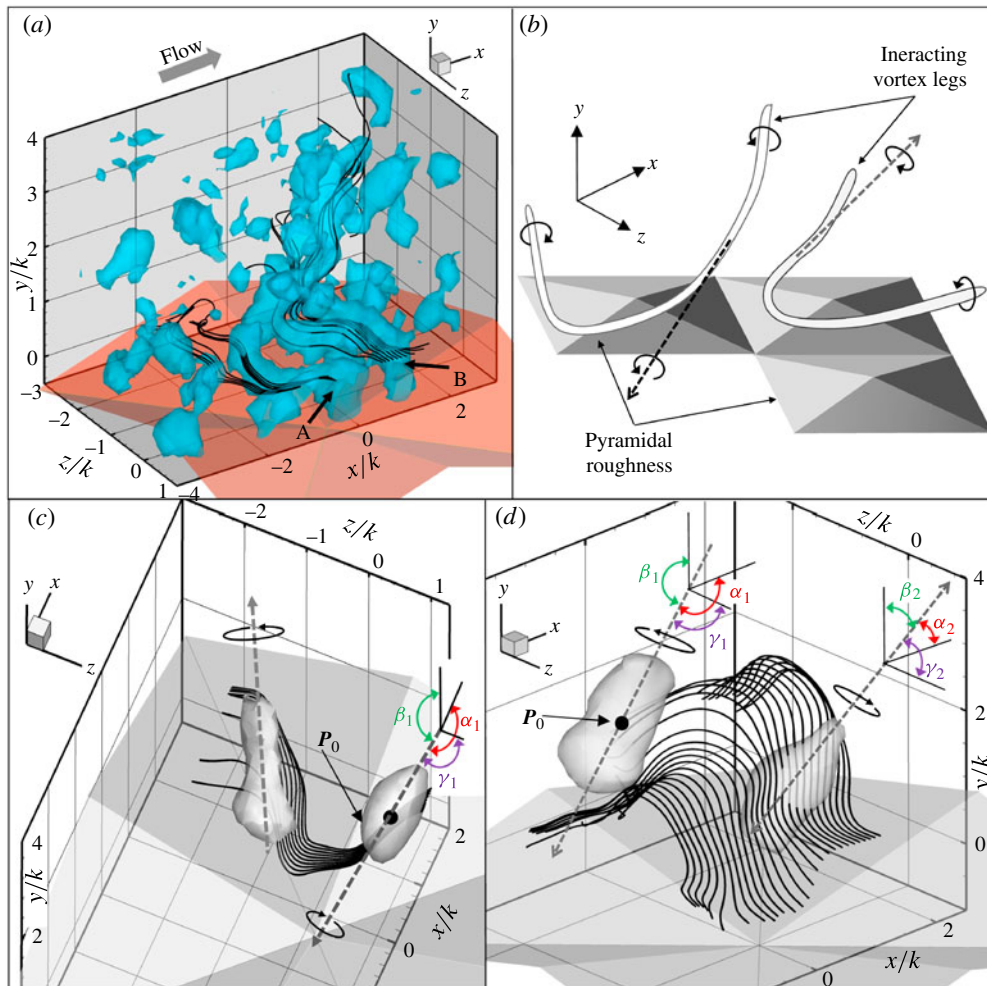
FIGURE 3. (a) A sample instantaneous realization, with iso-surface of $\lambda_2 = -1.5 \times 10^6 \text{ s}^{-2}$ and associated vortex lines (black); (b) depiction of ejection caused by interaction among U-shaped structures generated above neighbouring pyramids; and (c,d) coherent structures illustrated by iso-surfaces of $\{\lambda_2\}$ and sample vortex lines in LSE-based flow fields using the conditions (c) $\lambda_2 < 0$ at (1, 1.1, 0.6) and (d) $\lambda_2 < 0$ and $\omega_x < 0$ at (0, 2.1, −2).

dimensional data due the >0.5 mm depth of the laser sheet, which decreases terms involving v' (Ligrani & Moffat 1986; Hong *et al.* 2011). Enlarging the interpolation volume and using simple averaging reduces the largest discrepancies in $\overline{\langle u'v' \rangle}$ and $\overline{\langle v'v' \rangle}$ by 30 % and 50 %, respectively.

3.2. *Characteristic turbulent flow structures*

Figure 3(a) shows an instantaneous sample containing vortex lines and iso-surfaces of λ_2 (Jeong & Hussain 1995). The boundaries of the sample volume and the pyramidal elements within it are also displayed. It contains low-lying spanwise vortices, e.g. 'A', and a structure, marked 'B', that is in part aligned in the spanwise direction, and in part inclined at a sharp angle of 56° to the streamwise direction with little spanwise

inclination. This angle is determined from the eigen direction of the second-order moment of points with $\lambda_2 < -4 \times 10^{-6}$ s^{-2} ($\pm 4.5\%$ based on varying this threshold). The characteristic lengths of vortex fragments fall in the k–$3k$ range, although the total length of the inclined structure exceeds $4k$. Abruptly lifted structures that extend over a substantial fraction of the sample volume are evident only in 8% of the 850 realizations. However, 66% of the realizations contain similarly inclined smaller vortices, with characteristic length of k–$3k$. At $y/k < 1$, most realizations contain low-lying vortices, some with spanwise orientations, and others aligned nearly parallel to the rough-wall groove lines. In most cases (but not all), vortices aligned with grooves have preferred ω_x signs, with $\omega_x < 0$ in vortices located above grooves oriented at 45° to the x-axis, and $\omega_x > 0$ above grooves oriented at 135°. In some cases (not shown), spanwise structures appearing above the ridgeline start wrapping around the pyramid peak, presumably due to the pyramid-induced flow channelling.

   The U-shaped structures postulated in Hong *et al.* (2012), based on interpretation of two-dimensional PIV data, are illustrated in figure 3(*b*). They conjecture that these structures form as spanwise vortices, 'wrap' around the pyramid peaks and are stretched by the faster channelling flow between the ridgelines. The term 'wrap' might be misleading since the stretching and lifting occur above the roughness elements due to the non-uniform flow induced by the rough surface. When vortical legs generated above neighbouring elements appear simultaneously, they induce an ejection flow, which raises these legs. To determine the existence, statistical significance, orientation and interactions among structures prevalent in the inner layer, we first utilize LSE (Adrian & Moin 1988). Denoted with { }, the values of $\{u'_i\}$, $\{\partial u'_i/\partial x_j\}$, $\{\omega'_i\}$ and $\{\lambda_2\}$ at any point $\boldsymbol{P}$ in the sample volume, conditioned on $\lambda_2 < 0$ at another prescribed point $\boldsymbol{P}_0$, are estimated using:

$$\{u'_i(\boldsymbol{P})\} = \langle u'_i(\boldsymbol{P})|\lambda_2(\boldsymbol{P}_0) < 0 \rangle = \frac{\langle u'(\boldsymbol{P})\lambda_2(\boldsymbol{P}_0)\rangle}{\langle \lambda_2(\boldsymbol{P}_0)\lambda_2(\boldsymbol{P}_0)\rangle}\lambda_2(\boldsymbol{P}_0). \tag{3.1}$$

Figure 3(*c*) shows iso-surfaces of $\{\lambda_2\}$ and selected vortex lines for LSE based on the condition that $\lambda_2 < 0$ at $\boldsymbol{P}_0/k = (1, 1.1, 0.6)$, which is intentionally located on one side of the ridgeline. A total of 330 realizations, 39% of the dataset, satisfy this condition. A quasi-streamwise inclined structure centred around $\boldsymbol{P}_0$ with $\{\omega'_x\} < 0$, $\{\omega'_y\} < 0$, and $\{\omega'_z\} < 0$ becomes evident. Its angles with the coordinate system are ($\alpha_1 = 133°$, $\beta_1 = 119°$, $\gamma_1 = 123°$). More importantly, reducing the $\{\lambda_2\}$ level from -1.0×10^6 to -0.4×10^6 s^{-2} brings about another structure, with $\{\omega'_x\} > 0$, $\{\omega'_y\} > 0$, and $\{\omega'_z\} < 0$, on the other side of the ridgeline. The vortex lines connecting these two counter-rotating vortices 'wrap' around the region located above the forward face of the pyramid, creating a U-shaped structure inducing a downward flow between its legs.

   To identify the mechanism causing the lifting of the quasi-streamwise structures, we perform another conditional analysis, based on $\lambda_2 < 0$ and $\omega_x < 0$ at $\boldsymbol{P}_0/k = (0, 2.1, -2)$. This point is located in an area that would be occupied by the leg of a vortex generated by the pyramid centred at $(0, 0, -3.48)$. With 102 realizations (12% of dataset) satisfying this condition and using the same $\{\lambda_2\}$ threshold, the flow (figure 3*d*) consists of two structures. The first, with the expected $\{\omega'_x\} < 0$ and $\{\omega'_y\} < 0$, surrounds the conditioning point. Its $\{\lambda_2\}$ iso-surface has an orientation of ($\alpha_1 = 116°$, $\beta_1 = 149°$, $\gamma_1 = 105°$). The second, counter-rotating structure ($\{\omega'_x\} > 0$, $\{\omega'_y\} > 0$) is also aligned at a steep angle ($\alpha_2 = 65°$, $\beta_2 = 31°$, $\gamma_2 = 107°$). It appears at a lower elevation, between the ridgeline at $z = 0$, and the first vortex. As the vortex lines confirm, an upward (ejection) flow develops between these vortices. Hence, the presence of a quasi-streamwise structure generated around a pyramid is preferentially
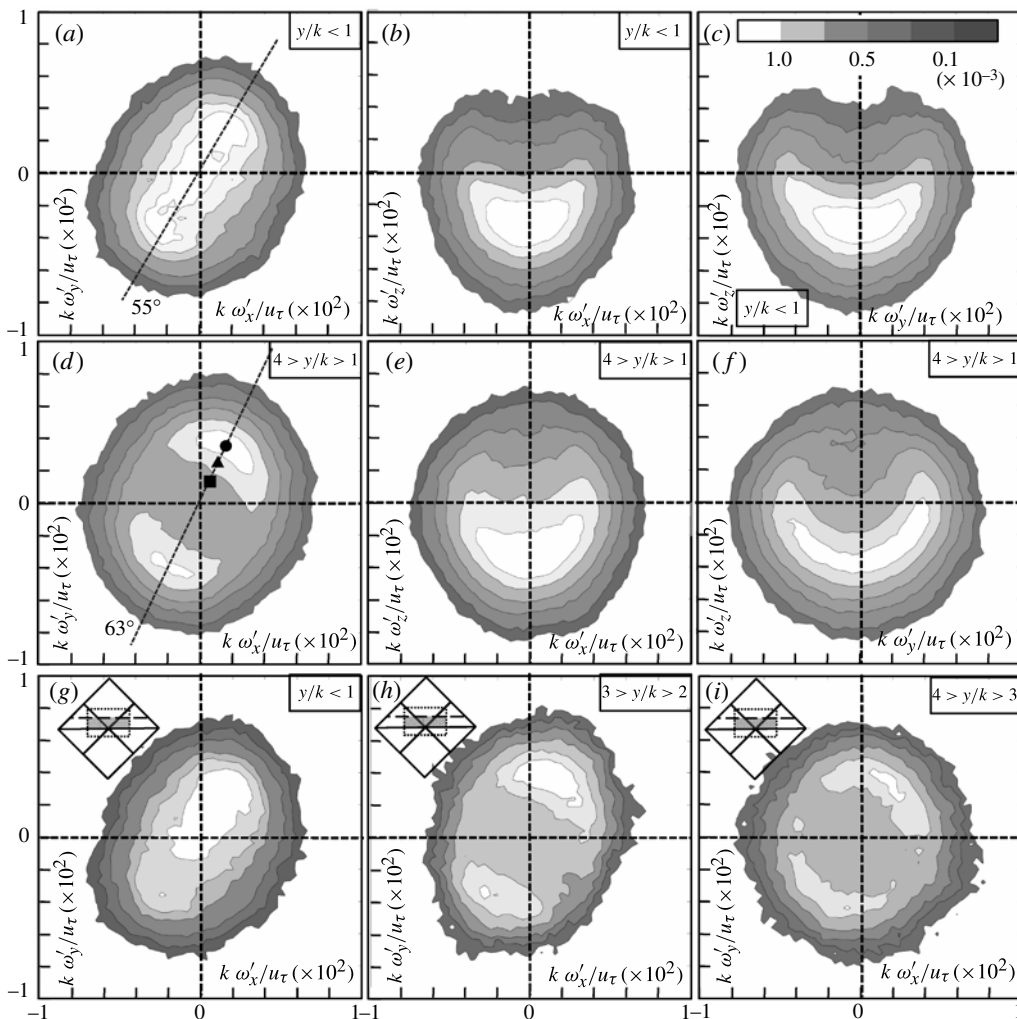
FIGURE 4. Joint p.d.f.s of vorticity components conditioned on $\lambda_2 < -1.5 \times 10^6$ s^{-2} for $y/k < 1$ (*a*–*c*), and $1 < y/k < 4$ (*d*–*f*). In (*g*–*i*) the spanwise extent is $-1.77 < z/k < 0$, as indicated, with $y/k < 1$ in (*g*), $2 < y/k < 3$ in (*h*), and $3 < y/k < 4$ in (*i*). Effect of the λ_2 threshold on the centre of the highest probability level for ($\omega'_x > 0$, $\omega'_y > 0$) is demonstrated in (*d*), with ●, $\lambda_2 < -1.5 \times 10^6$ s^{-2}; ▲, $\lambda_2 < -1 \times 10^6$ s^{-2}; and ■, $\lambda_2 < 0$.

associated with a counter-rotating vortex generated above the neighbouring pyramid. Thus, the interaction between legs of adjacent U-shaped vortices is statistically significant.

As the next step, figure 4(*a*–*f*) shows joint probability distribution functions (p.d.f.s) of ω'_i for data points satisfying $\lambda_2 < -1.5 \times 10^6$ s^{-2}, representing 11% of all data points with the strongest vortical structures. For $y/k < 1$ (figure 4*a*–*d*), the most probable $k\omega'_z/u_\tau$ is -0.0032, while the other components fluctuate between -0.0025 and 0.0025, indicating that most of the structures have significant spanwise component. There is, however, a clearly preferred ω_y/ω_x ratio, indicating that vortices with varying strengths and spanwise inclination still have a preferred x–y orientation of $55°$.

For $1 < y/k < 4$ (figure 4*d–f*), the crescent-shaped $\omega'_y - \omega'_z$ p.d.f. indicates that when $|\omega'_z|$ is high, $|\omega'_y|$ is low, i.e. the vortex is aligned in a horizontal plane. The accompanying $\omega'_x - \omega'_z$ p.d.f. indicates that the corresponding $|\omega'_x|$ is also low, i.e. the structure is predominantly a spanwise vortex. The crescents also indicate that when $|\omega'_y|$ and $|\omega'_x|$ are high, $|\omega'_z|$ is preferentially low, i.e. it is a quasi-streamwise vortex, whose distinct alignment angle of $63°$ is shown in figure 4(*d*). Thus, at $1 < y/k < 4$, the sublayer contains both spanwise structures and quasi-streamwise vortices with sharp inclinations. These results are consistent with the trends observed in instantaneous realizations.

Reducing the λ_2 threshold level, but still remaining within vortices ($\lambda_2 < 0$), shifts the centre of the most probable points to lower values, but the alignment remains unchanged, as demonstrated for positive ω'_x and ω'_y in figure 4(*d*). Repeating the analysis for the entire data set changes the p.d.f.s into circular shapes (not shown) with centres at $\omega'_y = \omega'_x = 0$, and $\omega'_z < 0$. The preferred signs of ω'_y and ω'_x depend on the measurement location relative to the ridgeline of the pyramid. When the spanwise extent is limited to $-1.77 < z/k < 0$ (figure 4*g–i*), i.e. to one side of the ridgeline, there is a clear bias towards structures with positive ω'_y and ω'_x at all elevations, while structures with $\omega'_y < 0$ and $\omega'_x < 0$ preferentially form on the other side of the ridgeline (data not shown). These trends are consistent with the signs of vorticity in the legs of the U-shaped structures depicted in figure 3(*b*). They also agree with the typical orientation of vortices observed in instantaneous realizations. Since the total sample volume covers slightly less space to the right of ridgelines, the overall p.d.f. peaks with positive ω'_y and ω'_x are higher (figure 4*a–f*). Finally, note that the most probable alignments agree with the LSE results. At $\boldsymbol{P}_0/k = (1, 1.1, 0.6)$ in figure 3(*c*), the *x–y* plane projection of vorticity is aligned at $180° + 54°$, and at $\boldsymbol{P}_0/k = (0, 2.1, -2)$ in figure 3(*d*), the angle is $62°$.

4. Discussion and conclusions

Statistical analysis of high-resolution three-dimensional velocity distributions, obtained using holographic microscopy, identifies structures dominating the inner part of a boundary layer over a pyramidal rough wall. The results demonstrate that a counter-rotating pair of sharply inclined quasi-streamwise vortices with downward flow (sweep) between them forms across the pyramid ridgeline (figure 3*c*). They are connected at low elevations above the forward face of the pyramid by a spanwise vortex section, creating the U-shaped structure conjectured in Hong *et al.* (2012). To a great part because of the location and dimensions of the sample volume, in instantaneous realizations, we often see only one of the legs of the same U-shaped vortex, some of which (8 %) are quite powerful (figure 3*a*). Also, 7 % of the instantaneous realizations show spanwise vortices beginning to form a U shape above the ridgeline. However, fragments of vortices with orientation and directions of rotation consistent with those of the U-shaped structures are evident in a majority of the realizations.

Combining the present data with the two-dimensional velocity distribution in Hong *et al.* (2011, 2012) enables us to propose the mechanism causing the formation and lifting of these structures. The preferred location for initial rollup of spanwise vorticity into vortices occurs along the ridgeline, at $y/k < 2$, near the point of minimum streamwise velocity above the forward face of the pyramid. Once formed, the roughness-induced flow channelling stretches the legs of these vortices axially along the space between ridgelines, forming the U-shaped structures (figure 3*b*).

Time-resolved two-dimensional PIV data (Hong *et al.* 2012) show that these vortices preferentially form and occasionally become powerful under large-scale sweeps, which increase the local near-wall shear strain. The analysis also suggests that interaction among counter-rotating legs generated by neighbouring pyramids, as shown in figure 3(*d*), induces ejections, which align the quasi-streamwise legs at steep angles ranging from 54° to 63°. The strain fields associated with relatively few (5 %) powerful interacting neighbouring legs are primary contributors to the SGS energy flux in the roughness sublayer (Hong *et al.* 2012).

Our findings bring up several issues. First, the formation and lifting of structures are enhanced by the effect of 'image vortices' (wall effect). Ignoring the surface details, the spanwise base of a U-shaped vortex is slowed by its image, enhancing the effect of flow channelling. Flow induced by the images of legs of the same structure separates these legs, bringing them closer to neighbouring vortices, which enhances the induced lifting.

Second, extending the discussion to general rough surfaces, any roughness protruding into the flow would cause local flow channelling and formation of so-called necklace vortices, similar to the present U shape. Such structures have been observed to form, e.g. around hemispherical roughness elements, by Yang & Wang (2009). Co-existence of 'head-down' hairpins with 'regular' hairpin structures has also been observed in large-eddy simulation of a canopy flow (Finnigan, Shaw & Patton 2009). The roughness geometry would presumably impact on the strength of individual structures, while the distance between elements would impact on the induced ejection, alignment of structures and interactions with the outer layer. For instance, we can postulate that increasing the gap between the roughness elements would result in weaker interactions among vortices generated above neighbouring elements, causing shallower inclination angles and less frequent ejections. Also, over surfaces with randomly distributed roughness, vortical interactions might have a broad spectral signature, unlike the present case, where periodicity imposes a distinct signature (Hong *et al.* 2012). These claims will be investigated in future studies.

Third, it would be of interest to discuss the relationship between the present findings and the development of coherent structures over smooth walls. Several mechanisms have been proposed for the 'regenerative' process that sustains the formation of vortices above smooth walls. For example, Adrian (2007) discuss the 'parent–offspring hairpin vortex regenerative scheme'. Schoppa & Hussain (2002) investigate a set of mechanisms involving local instabilities of a quasi-steady base flow, where the formation of coherent structures is triggered by a feedback induced by prior vortices. For these instabilities to occur, the inner-layer dynamics can be treated as autonomous, in agreement with the numerical results of e.g. Jimenez & Pinelli (1999). The present paper shows that in the roughness sublayer, the roughness elements create the spatial flow non-uniformities and associated instabilities needed for sustaining the formation of new structures. Included are: (*a*) the elevated streamwise velocity between pyramid ridgelines, which stretches the vortex legs; and (*b*) the region with minimum velocity along the ridgeline, above the forward face of the pyramid, where the initial rollup of structures occurs. The latter is the site of peak streamwise flow contraction ($\partial \langle u \rangle / \partial x < 0$) and consequently, maximum streamwise velocity fluctuations and turbulent kinetic energy production (Hong *et al.* 2011). However, the rollup of vortices and high SGS flux in the roughness sublayer preferentially occur under large-scale sweeps (Hong *et al.* 2012). This observation implies that previously generated large-scale structures do trigger the formation of new ones, suggesting that

rollup of U-shaped vortices occurs as outer-layer turbulence interacts with instabilities induced by the roughness elements.

Acknowledgements

REFERENCES

ADRIAN, R. J. 2007 Hairpin vortex organization in wall turbulence. *Phys. Fluids* **19**, 041301.

ADRIAN, R. J. & MOIN, P. 1988 Stochastic estimation of organized turbulent structure: homogeneous shear flow. *J. Fluid Mech.* **190**, 531–559.

ANTONIA, R. A. & LUXTON, R. E. 1971 The response of a turbulent boundary layer to a step change in surface roughness. Part 1. Smooth to rough. *J. Fluid Mech.* **48**, 721–761.

FINNIGAN, J. J., SHAW, R. H. & PATTON, E. G. 2009 Turbulence structure above vegetation canopies. *J. Fluid Mech.* **637**, 387–424.

HONG, J., KATZ, J., MENEVEAU, C. & SCHULTZ, M. P. 2012 Coherent structures and associated subgrid-scale energy transfer in a rough-wall turbulent channel flow. *J. Fluid Mech.*, doi:10.1017/jfm.2012.403.

HONG, J., KATZ, J. & SCHULTZ, M. P. 2011 Near-wall turbulence statistics and flow structures over 3D roughness in a turbulent channel flow. *J. Fluid Mech.* **667**, 1–37.

IKEDA, T. & DURBIN, P. A. 2007 Direct simulations of a rough-wall channel flow. *J. Fluid Mech.* **571**, 235–263.

JEONG, J. & HUSSAIN, F. 1995 On the identification of a vortex. *J. Fluid Mech.* **285**, 69–94.

JIMENEZ, J. 2004 Turbulent flows over rough walls. *Annu. Rev. Fluid Mech.* **36**, 173–196.

JIMENEZ, J. & PINELLI, A. 1999 The autonomous cycle of near-wall turbulence. *J. Fluid Mech.* **389**, 335–359.

LIGRANI, P. M. & MOFFAT, R. J. 1986 Structure of transitionally rough and fully rough turbulent boundary layers. *J. Fluid Mech.* **162**, 69–98.

MONTY, J. P., ALLEN, J. J., LIEN, K. & CHONG, M. S. 2011 Modification of the large-scale features of high Reynolds number wall turbulence by passive surface obtrusions. *Exp. Fluids* **51**, 1755–1763.

RAUPACH, M. R., ANTONIA, T. A. & RAJAGOPALAN, S. 1991 Rough wall boundary layers. *Appl. Mech. Rev.* **44**, 1–25.

SCHOPPA, W. & HUSSAIN, F. 2002 Coherent structure generation in near-wall turbulence. *J. Fluid Mech.* **453**, 57–108.

SCHULTZ, M. P. & FLACK, K. A. 2009 Turbulent boundary layers on a systematically varied rough wall. *Phys. Fluids* **21**, 015104.

SHENG, J., MALKIEL, E. & KATZ, J. 2006 Digital holographic microscope for measuring 3D particle distribution and motions. *Appl. Opt.* **45**, 3893–3901.

SHENG, J., MALKIEL, E. & KATZ, J. 2008 Using digital holographic microscopy for simultaneous measurements of 3D near wall velocity and wall shear stress in a turbulent boundary layer. *Exp. Fluids* **45**, 1023–1035.

TACHIE, M. F., BERGSTROM, D. J. & BALACHANDAR, R. 2003 Roughness effects in low-Re_θ open channel turbulent boundary layers. *Exp. Fluids* **35**, 338–346.

TALAPATRA, S. & KATZ, J. 2012 Scope of microscopic inline digital holography for resolving the 3D flow in the roughness sublayer. *Meas. Sci. Technol.* (in press).

YANG, Q. & WANG, M. 2009 Computational study of roughness induced boundary-layer noise. *AIAA J.* **47**, 2417–2429.